Influence of solvent polarity on the structure of drop-cast electroactive tetra(aniline)-surfactant thin films

Electronic Supplementary Information

T. G. Dane,[a] J. E. Bartenstein,[a] B. Sironi,[a] B. M. Mills,[a] O. A. Bell,[a] J. E. Macdonald,[b] T. Arnold,[c] C. F. J. Faul[a] and W. H. Briscoe[a]

[a] School of Chemistry, University of Bristol, Bristol, BS8 1TS, UK.

[b] School of Physics and Astronomy, Cardiff University, Cardiff CF24 3AA, UK

[c] Diamond Light Source Ltd., Diamond House, Harwell Science and Innovation Campus, Didcot, Oxfordshire, UK

Contents

S1 AFM imaging

AFM images were acquired for all TANI(BEHP)$_{0.5}$ films prepared exactly as described in the Experimental section of the main text. The films were imaged in ambient conditions under the PeakForce tapping control mode using a Multimode VIII microscope with a Nanoscope V controller (Bruker, CA, USA). This was coupled with a high-speed scan unit and SCANASYST-AIR_HR cantilevers of nominal tip radius 2 nm and spring constant 0.4 N/m.

PeakForce Tapping is a non-resonant scanning mode which investigates the topography of a surface whilst maintaining a constant level of force interaction between the cantilever tip and the sample. The topographic images (top row in Fig. S1) represent the height of features, and the PeakForce error images (bottom row in Fig. S1) represent the deflection of the cantilever (*cf.* the amplitude channel in tapping mode and the deflection channel in contact mode).

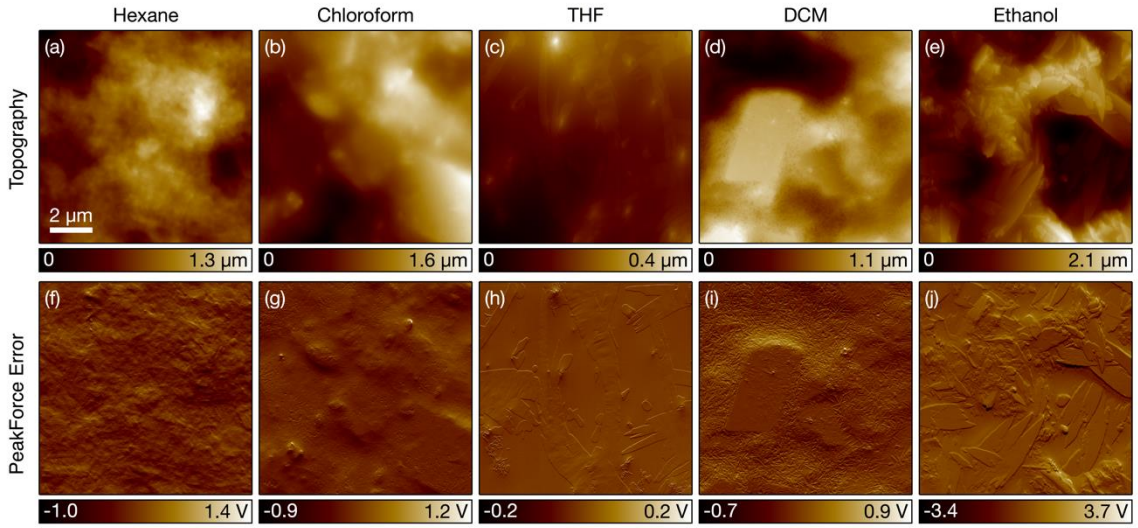

Fig. S1 Topographic (a-e, top row) and corresponding PeakForce error (f-j, bottom row) AFM images of TANI(BEHP)$_{0.5}$ films cast from hexane (a, f), chloroform (b, g), THF (c, h), DCM (d, i), and ethanol (e, j). The minimum and maximum *z*-values of the false colour images are indicated in the scale bar beneath each image. The field of view for each image is 10×10 μm^2.

S2 Regions of interest used for line profile extraction

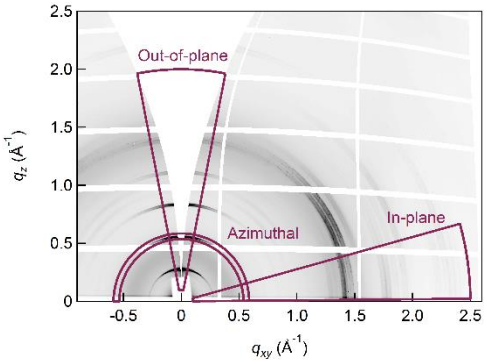

Fig. S2 Integration regions used for extracting out-of-plane, in-plane and Azimuthal line profiles.

S3 Discussion of the overlapping reflections for the DCM- and ethanol cast films

The enlarged views of the regions around the (20) reflections in Fig S2 show clearly that the reflections are in fact composed of two very closely overlapping peaks for the ethanol and DCM. Cast films. By contrast, for the hexane cast film (as well as the THF- and chloroform films), it is clear that there is only one distinct peak.

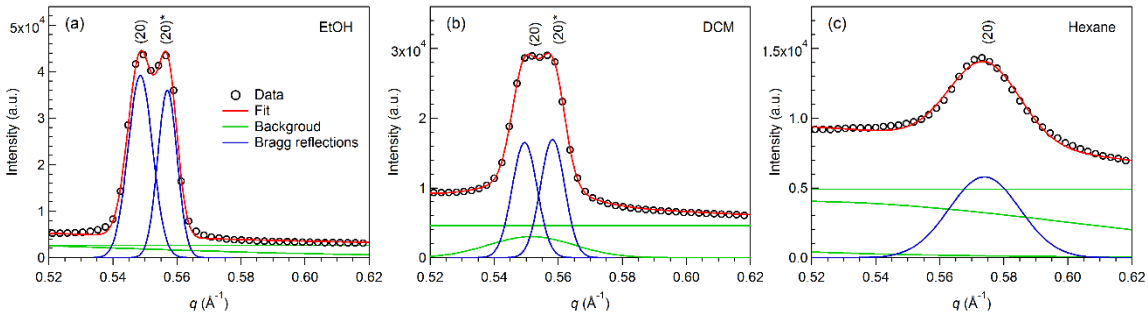

Fig. S3 Enlarged views of the 1D out-of-plane line profiles from Fig. 3 in the main text (and Fig. S4 of the ESI) for the films cast from (a) ethanol, (b) DCM and (c) hexane.

In GIXD experiments, if the incident angle is close to the critical angle of the substrate but greater than the critical angle of the film, the transmitted beam penetrates the film and reflects from the substrate. This reflected beam can act as a second source of illumination and is diffracted by the film upon exiting. This causes a superposition in the diffraction patterns of the diffraction from the incoming beam and the outgoing substrate-reflected beam, whereby the two diffraction patterns are offset approximately by the incident angle (neglecting refraction effects).[1] The GIXD patterns for the ethanol-cast film as a function of incident angle shown in Fig. S3 show clearly this effect. The (10) reflections from the incoming beam remain at a fixed position in q_z (white dashed line), whereas the (10) reflections from the substrate-reflected beam occur at a greater q_z value, which is dependent on the incident angle (black arrows).

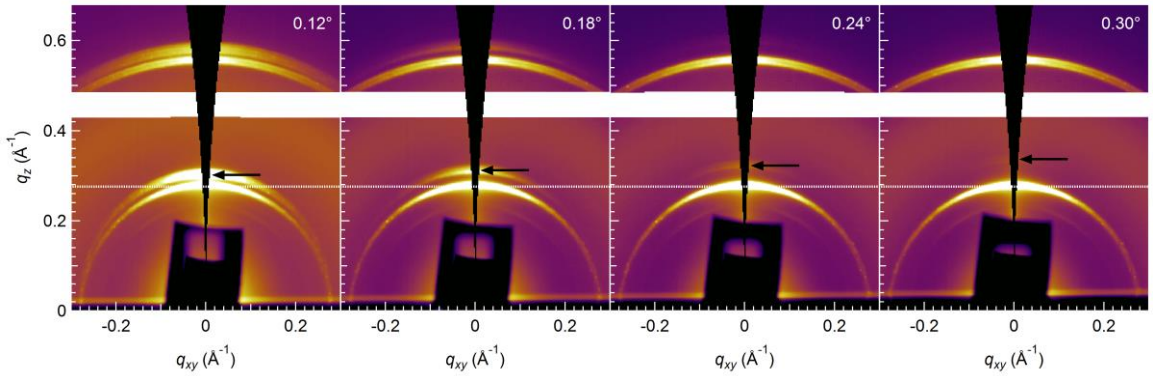

Fig. S4 GIXD patterns for the ethanol-cast TANI(BEHP)$_{0.5}$ film recorded at increasing incident angles α_i of 0.12°, 0.18°, 0.24°, and 0.30° (labelled in top right hand corner of each pattern). The (10) reflections occur at a fixed q_z value (indicated by the dashed horizontal line) whereas the (10) reflections originating from the substrate-reflected beam are labelled with black arrows.

The intensity of the substrate-reflected diffraction features decays rapidly as the incident angle is increased, as the intensity of the reflected beam decays with θ^{-4} as given by the Fresnel equations.[2] The data presented in Fig 3 of the main text were recorded at $\alpha_i = 0.36°$. At this point the intensity of the diffraction features arising from the reflected beam is too weak to be detected. Furthermore, the offset between the two peaks, should they arise from the reflected beam, would be $\Delta q \sim 0.06$ Å^{-1}, whereas they are much closer together at $\Delta q < 0.01$ Å^{-1}, and this offset is not dependent on the incident angle. We therefore propose that the source of these split reflections is either polymorphism or due to the large footprint of the beam.

S4 GIXD line profile fitting

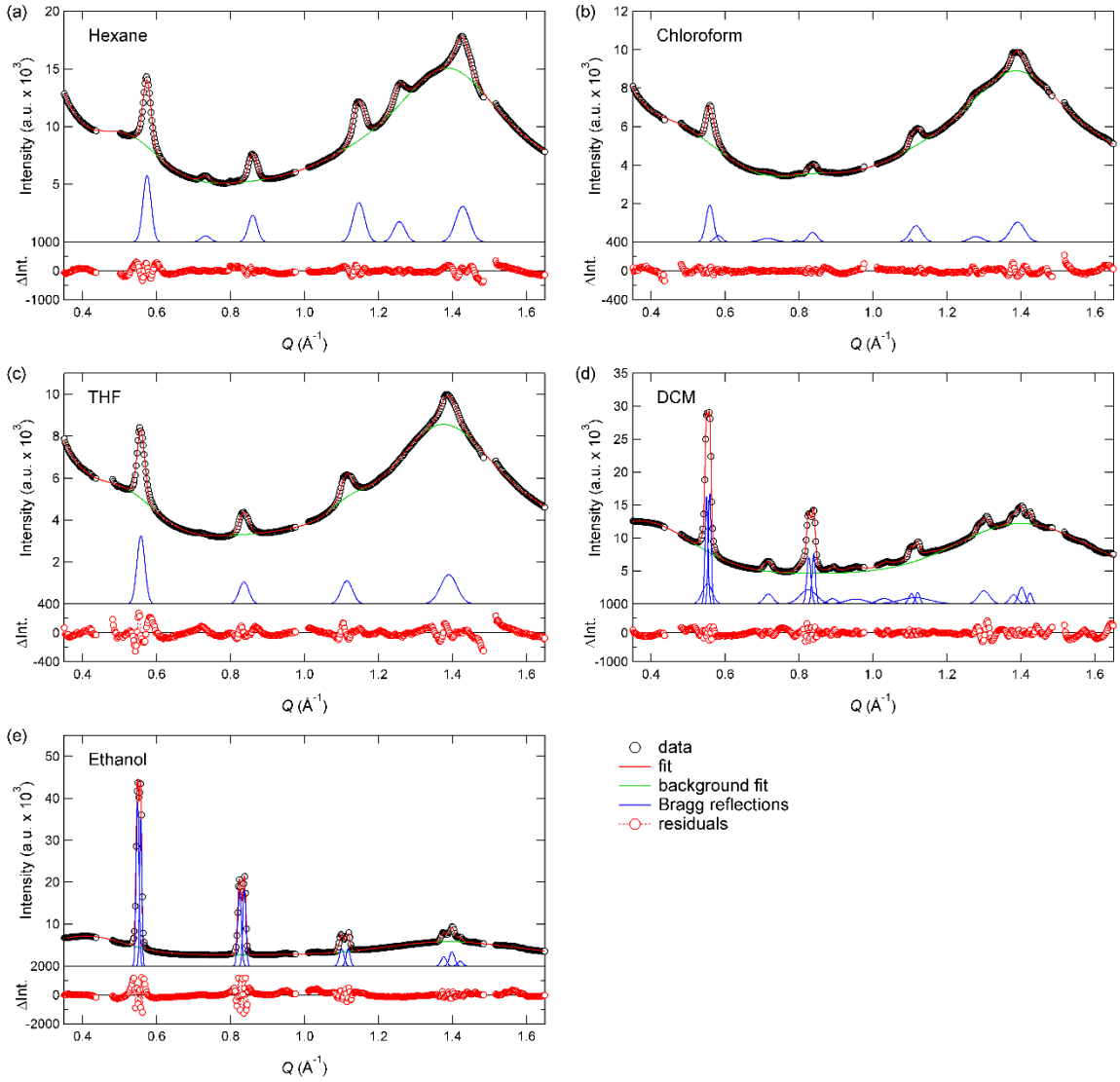

Fig. S5 Summary of fitted GIXD patterns for TANI(BEHP)$_{0.5}$ films cast from (a) hexane, (b) chloroform, (c) THF, (d) DCM, and (e) ethanol.

S5 Domain size and paracrystallinity determination

S5.1 Theoretical basis

According to Hosemann & Hindeleh[3] and Wu *et al.*,[4] the measured full-width at half maximum (FWHM) of a Bragg reflection, δ, can be separated into two components: line broadening due to finite crystallite size (δ_C) and broadening due to paracrystalline disorder (δ_β), *i.e.*, the fluctuation of the lattice spacing about the mean value d through

$$\delta^2 = \delta_C^2 + \delta_\beta^2 \tag{1}$$

The finite crystallite size, L_a is related to δ_C through the Scherrer equation

$$\delta_C = \frac{K}{L_a} \tag{2}$$

where K is a shape factor (typically $K = 0.9$). The paracrystalline disorder parameter, g, is a measure of the distribution of the lattice spacing (Δd) expressed as a fraction of d. The line broadening due to g is given by (see references [3] and [4] for full derivation):

$$\delta_\beta = \frac{(\pi g n)^2}{d} \tag{3}$$

where n is the reflection order along the crystallographic axis (*i.e.* for a reflection series along (h00), $n = h = 1, 2, 3, \ldots$). Thus the measured FWHM of a Bragg reflection can be expressed as:

$$\delta^2 = \left(\frac{K}{L_a}\right)^2 + \frac{(\pi g n)^4}{d^2} \tag{4}$$

Thus if one determines the FWHM (δ) for a series of reflections (with order n) and fits a linear regression to δ^2 *vs* n^4, L_a can be determined from the intercept and g from the slope.

Wu *et al.* perform all of their calculations in s-space (the scattering vector) where

$$s = 2 \sin \theta / \lambda \tag{5}$$

The wavevector transfer is therefore related to s through

$$q = s/2\pi \tag{6}$$

To reformulate Equation (4) in q-space, one arrives at:

$$\frac{\Delta q^2}{(2\pi)^2} = \left(\frac{0.9}{L_a}\right)^2 + \frac{(\pi g)^4}{d^2} \cdot n^4 \tag{7}$$

where Δq is the measured FWHM of a Bragg reflection. Fitting a linear regression of the form $y = c + mx$, where

$$y = \frac{\Delta q^2}{(2\pi)^2} \tag{8}$$

$$x = n^4 \tag{9}$$

$$m = \frac{(\pi g)^4}{d^2} \tag{10}$$

$$c = \left(\frac{0.9}{L_a}\right)^2 \tag{11}$$

the L_a and g parameters are determined as follows:

$$L_a = \frac{0.9}{\sqrt{c}} \tag{12}$$

$$g = \frac{1}{\pi}(md^2)^{1/4} \tag{13}$$

S5.2 Error propagation

The calculated lattice spacing d determined from the fitted peak centred at q with error (standard deviation) of σ_q has an error σ_d given by:

$$\sigma_d = \frac{2\pi}{q^2} \cdot \sigma_q \tag{14}$$

The FWHM of a Bragg reflection (Δq) returned from peak fitting, with an error of $\sigma_{\Delta q}$, the error in y for the paracrystalline plots given by Equation (8) is:

$$\sigma_y = \frac{\Delta q}{2\pi^2} \cdot \sigma_{\Delta q} \tag{15}$$

Fitting a linear regression to y *vs* n^4 gives errors in the gradient (m) and intercept (c) coefficients, σ_m and σ_c, respectively. The error in the L_a and g derived parameters is then given by

$$\sigma_{L_a} = -0.45c^{-3/2} \cdot \sigma_c \tag{16}$$

$$\begin{aligned} \sigma_g &= \left[\left(\frac{1}{4\pi} d^{\frac{1}{2}} m^{-\frac{3}{4}}\right)^2 (\sigma_m)^2 + \left(\frac{1}{2\pi} m^{\frac{1}{4}} d^{-\frac{1}{2}}\right)^2 (\sigma_d)^2\right]^{\frac{1}{2}} \\ &\approx \frac{1}{4\pi} d^{\frac{1}{2}} m^{-\frac{3}{4}} \sigma_m \end{aligned} \tag{17}$$

S5.3 Paracrystalline disorder plots

Fig. 4 in the main text shows the paracrystalline disorder plots for each sample. Here they are plotted separately for clarity on the same scale.

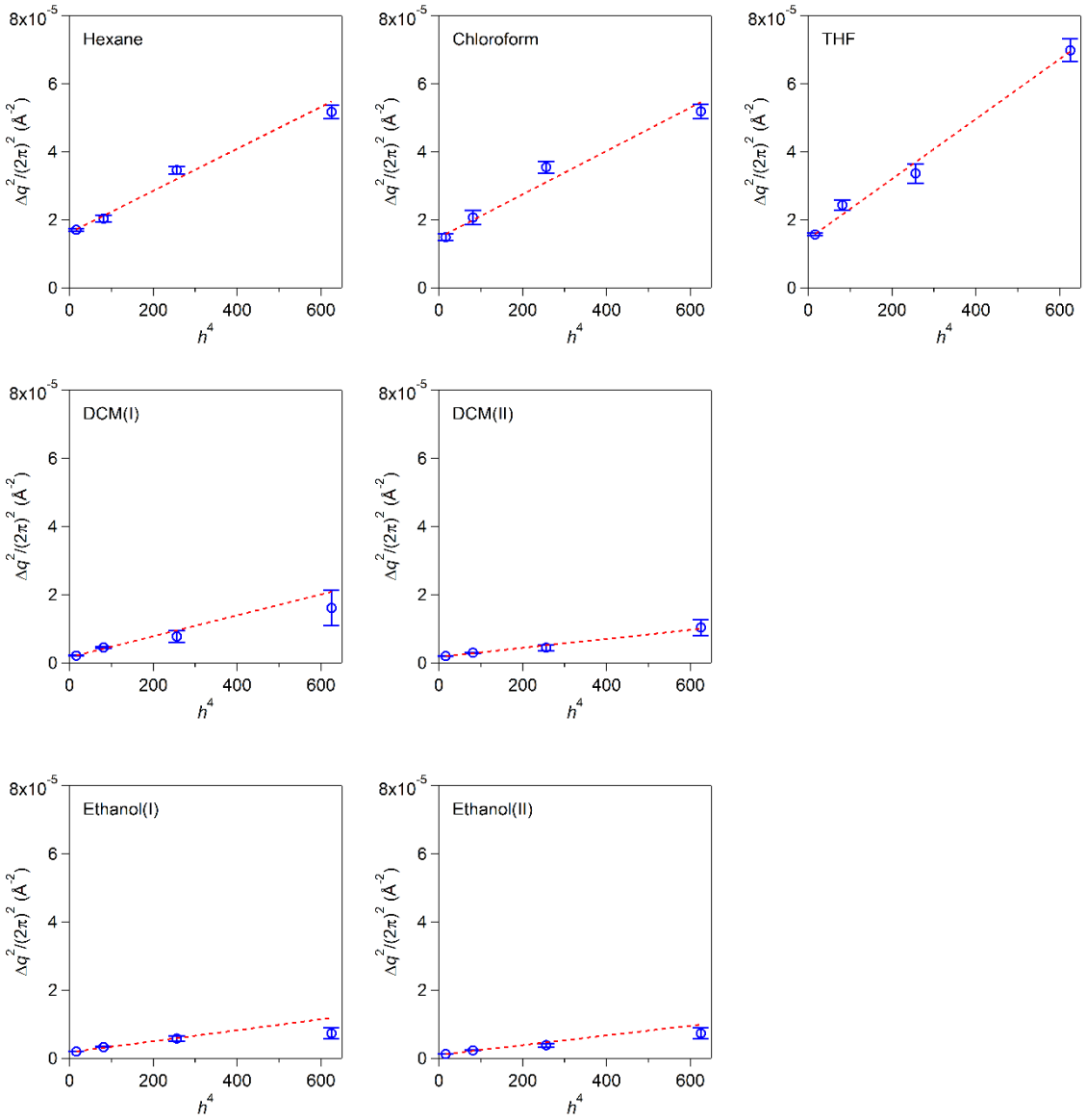

Fig. S6 Individual paracrystalline disorder plots for each sample plotted on the same scale. The (I) and (II) phases for the DCM and ethanol-cast films have been plotted separately.

S6 Correlation between solvent parameters and degree of order within the film

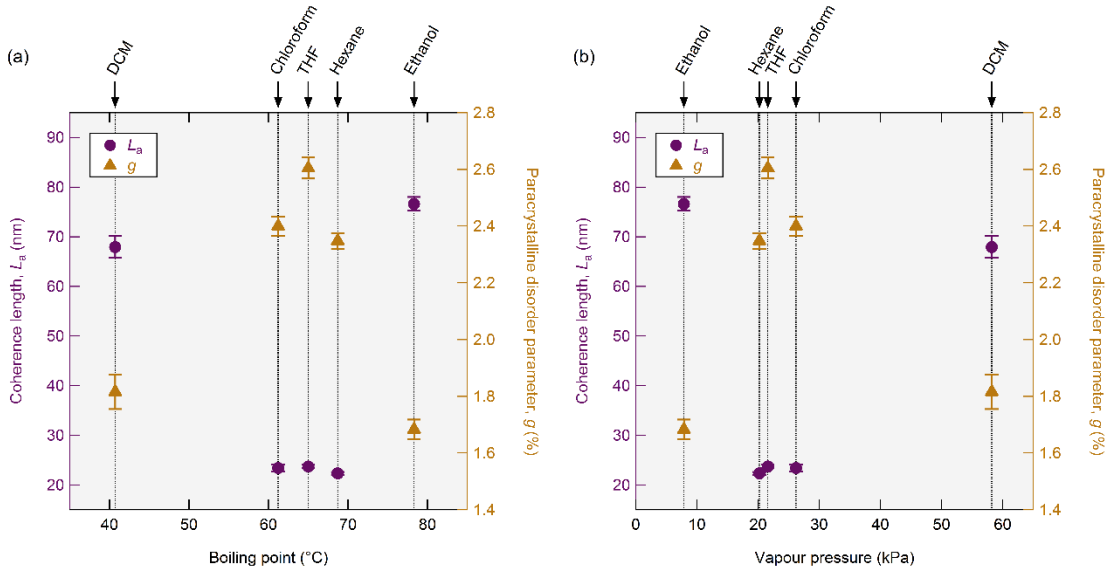

Fig. S7 Coherence length (purple circles) and paracrystalline disorder parameter (orange triangles) as a function of the boiling point (a) and vapour pressure (b) of the casting solvent.

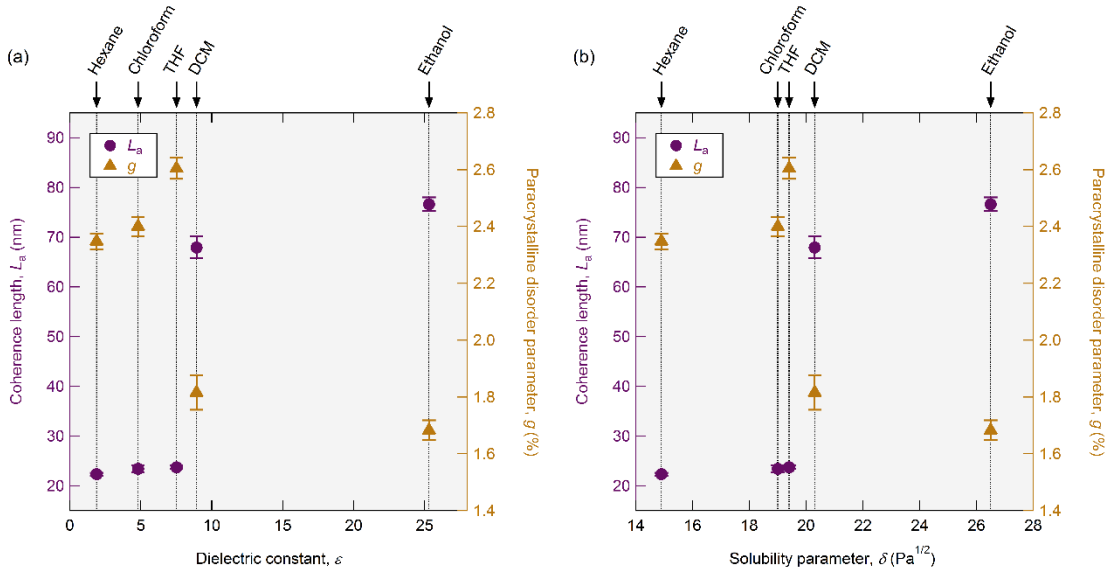

Fig. S8 Coherence length (purple circles) and paracrystalline disorder parameter (orange triangles) as a function of the dielectric constant (a) and total solubility parameter (b) of the casting solvent.

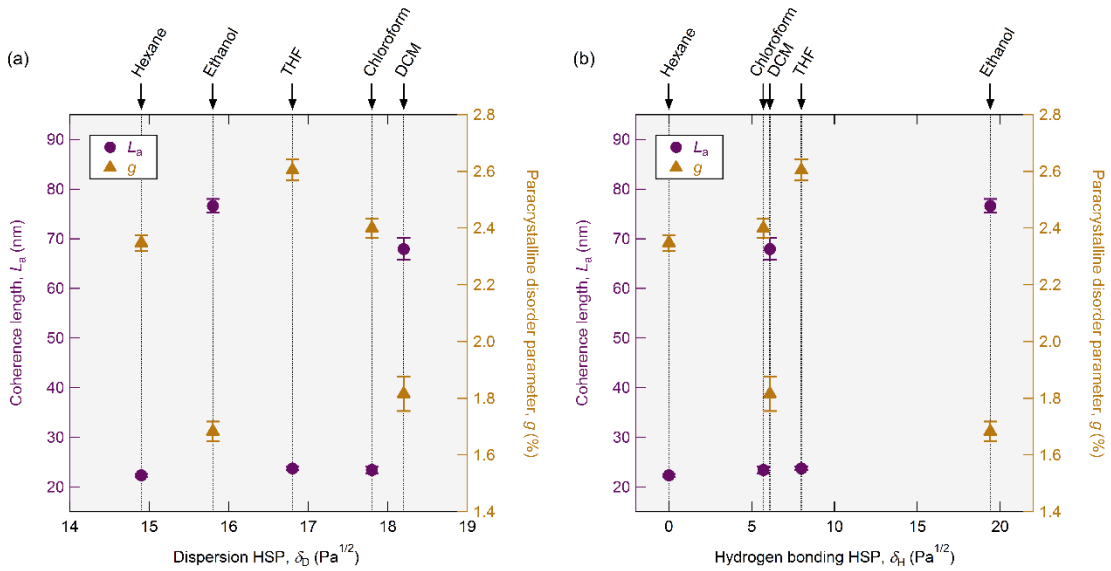

Fig. S9 Coherence length (purple circles) and paracrystalline disorder parameter (orange triangles) as a function of the dispersion HSP (a) and hydrogen bonding HSP (b) of the casting solvent.

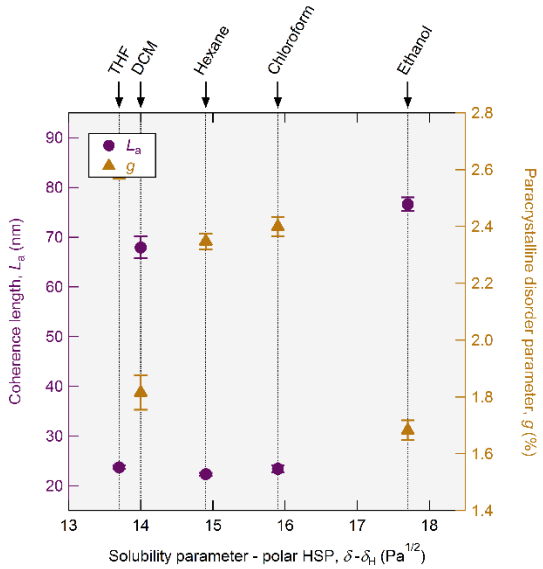

Fig. S10 Coherence length (purple circles) and paracrystalline disorder parameter (orange triangles) as a function of the total solubility parameter minus the polar HSP of the casting solvent.

S7 References

1 B. Lee, I. Park, J. Yoon, S. Park, J. Kim, K.-W. Kim, T. Chang and M. Ree, *Macromolecules*, 2005, **38**, 4311–4323.

2 J. Als-Nielsen and D. McMorrow, *Elements of Modern X-Ray Physics*, John Wiley & Sons Ltd, Chichester, United Kingdom, 2nd edn., 2011.

3 R. Hosemann and A. M. Hindeleh, *J. Macromol. Sci. - Phys.*, 1995, **B34**, 327–356.

4 T.-M. Wu, J. Blackwell and S. N. Chvalun, *Macromolecules*, 1995, **28**, 7349–7354.